JOURNAL OF SYNCHROTRON RADIATION

ISSN 1600-5775

Received 7 November 2020
Accepted 28 February 2021

Edited by P. A. Pianetta, SLAC National Accelerator Laboratory, USA

Keywords: spin detector; spin-filter effect; spin-resolved ARPES.

A new imaging concept in spin polarimetry based on the spin-filter effect

Oleg E. Tereshchenko,[a,b]* Vladimir A. Golyashov,[a,b] Vadim S. Rusetsky,[a,c] Andrey V. Mironov,[c] Alexander Yu. Demin[c] and Vladimir V. Aksenov[c]

[a]Rzhanov Institute of Semiconductor Physics, Siberian Branch, Russian Academy of Sciences, Novosibirsk 630090, Russian Federation, [b]Novosibirsk State University, Novosibirsk 630090, Russian Federation, and [c]CJSC EKRAN-FEP, Novosibirsk 630060, Russian Federation. *Correspondence e-mail: teresh@isp.nsc.ru

The concept of an imaging-type 3D spin detector, based on the combination of spin-exchange interactions in the ferromagnetic (FM) film and spin selectivity of the electron–photon conversion effect in a semiconductor heterostructure, is proposed and demonstrated on a model system. This novel multichannel concept is based on the idea of direct transfer of a 2D spin-polarized electron distribution to image cathodoluminescence (CL). The detector is a hybrid structure consisting of a thin magnetic layer deposited on a semiconductor structure allowing measurement of the spatial and polarization-dependent CL intensity from injected spin-polarized free electrons. The idea is to use spin-dependent electron transmission through in-plane magnetized FM film for in-plane spin detection by measuring the CL intensity from recombined electrons transmitted in the semiconductor. For the incoming electrons with out-of-plane spin polarization, the intensity of circularly polarized CL light can be detected from recombined polarized electrons with holes in the semiconductor. In order to demonstrate the ability of the solid-state spin detector in the image-type mode operation, a spin detector prototype was developed, which consists of a compact proximity focused vacuum tube with a spin-polarized electron source [*p*-GaAs(Cs,O)], a negative electron affinity (NEA) photocathode and the target [semiconductor heterostructure with quantum wells also with NEA]. The injection of polarized low-energy electrons into the target by varying the kinetic energy in the range 0.5–3.0 eV and up to 1.3 keV was studied in image-type mode. The figure of merit as a function of electron kinetic energy and the target temperature is determined. The spin asymmetry of the CL intensity in a ferromagnetic/semiconductor (FM-SC) junction provides a compact optical method for measuring spin polarization of free-electron beams in image-type mode. The FM-SC detector has the potential for realizing multichannel 3D vectorial reconstruction of spin polarization in momentum microscope and angle-resolved photoelectron spectroscopy systems.

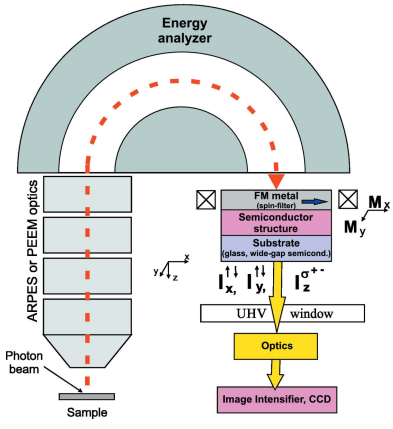

1. Introduction

1.1. Free-electron spin detection: from single- to multi-channel mode

1.1.1. Electron spin detection via spin–orbit interactions. Detection of electron spin with the efficiency of spin-integrated angular-resolved photoelectron spectroscopy (ARPES) is a major issue in modern photoelectron spectroscopy, which initiated the search for an 'ideal' spin filter for free electrons. The definition of an 'ideal' spin detector can be formulated in terms of the capability of high-efficiency multichannel (image-type) spin detection simultaneously with normal ARPES or momentum microscopy measurements. Spin detectors developed to date are based on the phenomena caused by spin–orbit interactions (SOIs) of the electron or the

spin-exchange interactions of ferromagnetic (FM) materials. The development of multichannel spin detectors has already begun and several advancements have been reported over the past ten years.

Despite the century-old history of the electron spin discovery, including the original work by Nevill Francis Mott (1929), the detection of free-electron spin has remained a challenge. One of the first electron spin detectors, still most widely used, is the Mott detector, which utilizes the phenomenon of asymmetric spin-polarized electron scattering in atoms as a result of SOIs [Mott detector, spin-polarized low-energy electron diffraction (SPLEED) detector] (Ghiringhelli *et al.*, 1999; Kirschner & Feder, 1979). Spin detectors based on spin–orbit scattering phenomena range from high-energy scattering ($E \sim 10^5$ eV) (Kisker *et al.*, 1982; Hoesch *et al.*, 2002; Petrov *et al.*, 2007) to low-energy scattering ($E \sim 102$ eV) (Kirschner & Feder, 1979; Sawler & Venus, 1991; Yu *et al.*, 2007). All present commercial Mott-type detectors (Yu *et al.*, 2007; Ghiringhelli *et al.*, 1999; Gay, 2009; Petrov *et al.*, 2007) are based on single-channel electron scattering and are characterized by a figure of merit (FOM) of typically 10^{-4}. This means the efficiency is four orders of magnitude lower than single-channel spin-integrated photoemission spectroscopy. One way to increase the efficiency of a Mott detector is conversion of a single-channel detector to an image-type detector. A promising concept of an iMott-based multichannel spin detector was proposed in combination with a normal hemispherical analyzer (Strocov *et al.*, 2015). The concept is based on the simultaneous 2D pattern registration by left-and-right or up-and-down detectors and subsequent evaluation of the spin-dependent asymmetry. 2D unpolarized images in an iMott detector have been demonstrated in previous work (Petrov *et al.*, 2020).

One of the disadvantages of the Mott detector is the high voltage of operation, which can be overcome by using the low-energy electron diffraction (LEED) method. The LEED spin detector based on a W single crystal (SPLEED detector) was developed (Kirschner, 1985) and used for spin-resolved photoemission without utilizing high voltage (Wang *et al.*, 1981). Unlike the Mott detector, the lifetime of the SPLEED detector is more sensitive to vacuum conditions and varies from a month (Vasilyev *et al.*, 2015) to a year (Kirschner, 2020). Subsequent development led to the creation of multi-channel detectors with the idea to use the scattering targets as a spin-polarizing electron mirror, opening the way to multi-channel spin analysis (reflection-type spin filters) (Tusche *et al.*, 2011). In these devices, the electron beam is specularly reflected from high-Z targets such as W(001) (Kolbe *et al.*, 2011), Ir(001) (Kutnyakhov *et al.*, 2013) and Au/Ir(001) (Kirschner *et al.*, 2013; Suga & Tusche, 2015), with intensities dependent on the spin polarization. The principle of this reflection-type spin filter is also SOI. The difference between the multichannel design and the Mott- and SPLEED-type detectors is the inherent lack of a left–right scattering asymmetry, meaning that the initial beam polarization should be inversed or experimental parameters have to be adjusted for a polarization analysis. The SPLEED-type spin filter is frequently used in several laboratories (Maaß *et al.*, 2016) and spin-ARPES endstations in the VUV-range at BESSY II, Berlin (Medjanik *et al.*, 2017); the XUV-range at ELETTRA, Trieste, Italy (Tusche *et al.*, 2018); the soft X-ray range at PETRA III, Hamburg, Germany (Vasilyev *et al.*, 2020); and the hard X-ray range at SPring-8, Hyogo, Japan (Kozina *et al.*, 2016). The latter work presents the only spin-resolved valence band measurement with hard X-rays existing so far, using the single-channel version of the SPLEED detector.

1.1.2. Electron spin detection via the spin-exchange interaction. Spin polarimeters based on an exchange interaction fall into three categories: those employing reflection (Tillmann *et al.*, 1989) or absorption (Erbudak & Müller, 1981; Pierce *et al.*, 1981), and those employing transmission (Pappas *et al.*, 1991; Schönhense & Siegmann, 1993; Lassailly *et al.*, 1994). At present, the most efficient spin polarimeters are based on 'very low' energy exchange scattering from an Fe(001) epitaxial film (Tillmann *et al.*, 1989) [very low-energy electron diffraction (VLEED) spin detector]. The reflectivity dependence on the relative alignment of the incoming electron's spin polarization and surface magnetization directions can be applied to spin polarimetry with nearly 50–100 times higher efficiency than Mott-polarimeters (Hillebrecht *et al.*, 2002; Okuda *et al.*, 2008; Bertacco *et al.*, 1999; Jozwiak *et al.*, 2010; Escher *et al.*, 2011; Bigi *et al.*, 2017). A multichannel spin detector using the VLEED technique is also being developed (Thiede *et al.*, 2014; Ji *et al.*, 2016). It has comparable characteristics as a single-channel detector but a much larger number of angle points have been obtained in an imaging-type exchange scattering spin polarimeter (Ji *et al.*, 2016). The lifetime of the VLEED detector is also relatively short (2–4 weeks) and requires surface refreshing of the target.

Currently, it appears that the general tendency in spin-ARPES follows the method of increasing the dimension of existing single-channel detectors, where the electron beam emitted from the sample is first projected onto the scattering target and then reconstructed onto the 2D electron sensitive detector. For this reason, all the disadvantages inherent in single-channel detectors are preserved to the same extent for detectors with spatial resolution (image-type) and, to date, 3D spin analysis using multichannel spin detectors has not been reported.

1.1.3. Spin-filter effect in thin ferromagnetic films. An alternative approach to measuring the spin polarization of an electron beam is to use a 'real filter' for injection of spin-polarized electrons in a magnetic film. Spin filters can act either as sources of polarized electrons or as polarimeters. Spin-dependent electron transmission through FM ultrathin films was proposed as a high-efficiency spin filter (Schönhense & Siegmann, 1993; Pappas *et al.*, 1991; Oberli *et al.*, 1998; Lassailly *et al.*, 1994). In the majority of experiments, spin-dependent transmission was studied in photoemission experiments by the so-called overlayer technique (Pappas *et al.*, 1991). The idea of a spin filter is similar to an optical linear polarizer. It was shown that the transmitted current depends on the relative orientation of the incident spin polarization with respect to the cobalt layer magnetization by measuring

the direct transmission of a spin polarized free-electron beam through a freestanding Au/Co/Au film (Oberli *et al.*, 1998; Lassailly *et al.*, 1994). Fig. 1(*a*) illustrates how to operate a spin filter (freestanding magnetic film). When an electron beam of spin polarization P_0 is injected into an ultrathin FM film, the transmitted current depends on the relative orientation of the incident spin polarization with respect to the film-saturated magnetization. One of the properties of the spin filter is that its spin selectivity depends on the energy of hot electrons traveling through the FM film. For the typical Au/Co/Au structure, the Sherman function value of such a spin filter was determined in the range 0.3–0.8 for low injection energy (5–10 eV) (Drouhin *et al.*, 1996; Oberli *et al.*, 1998).

1.1.4. Electrical spin detection in the ferromagnetic/semiconductor heterojunction. Devices based on a transmitted spin filter, although possible in principle, have the experimental problem of creating large, freestanding several-nanometre-thick films of FM layers. This technical problem can be solved by deposition of an FM film on the semiconductor substrate. In this case, the hot electrons are injected into a thin magnetic film and the current transmitted through the film is detected in the semiconductor. This process can be considered as the opposite to that used in the photoemission overlayer technique (Pappas *et al.*, 1991). The transmitted current exhibits a spin asymmetry, which is measured by reversing the incident electron polarization and/or the magnetization state of the film (Filippe *et al.*, 1998; Tereshchenko *et al.*, 2011). As has been shown, it is quite feasible to measure the integral polarization of a free-electron beam using electron injection into a Pd/Fe/GaAs(001) heterostructure with a magnetic Schottky barrier (SHB) at an efficiency equal to the Mott detector. The current of the electrons that passed through an FM film to the semiconductor was measured. The magnetic film acts as a spin filter while the SHB at the interface plays the selector role, allowing mainly the electrons with their spin projection on the direction collinear to the opposite magnetization vector of FM layer to pass through [Fig. 1(*b*)]. Thus, it is possible to determine the spin polarization of the electron beam by measuring the difference between the currents of the injected electrons with opposite magnetizations of the film. The main difficulty for manufacturing an ferromagnetic/semiconductor (FM-SC) structure is the construction of an FM/GaAs interface with a low density of defects and surface states since the detector demands a magnetic SHB of a considerably large area (1 cm^2) and concurrently low leakage currents (10^{-7} A cm^{-2}) (Tereshchenko *et al.*, 2011, 2012). Another major shortcoming is that the current mode [Fig. 1(*b*)] fails to record a spatial distribu-

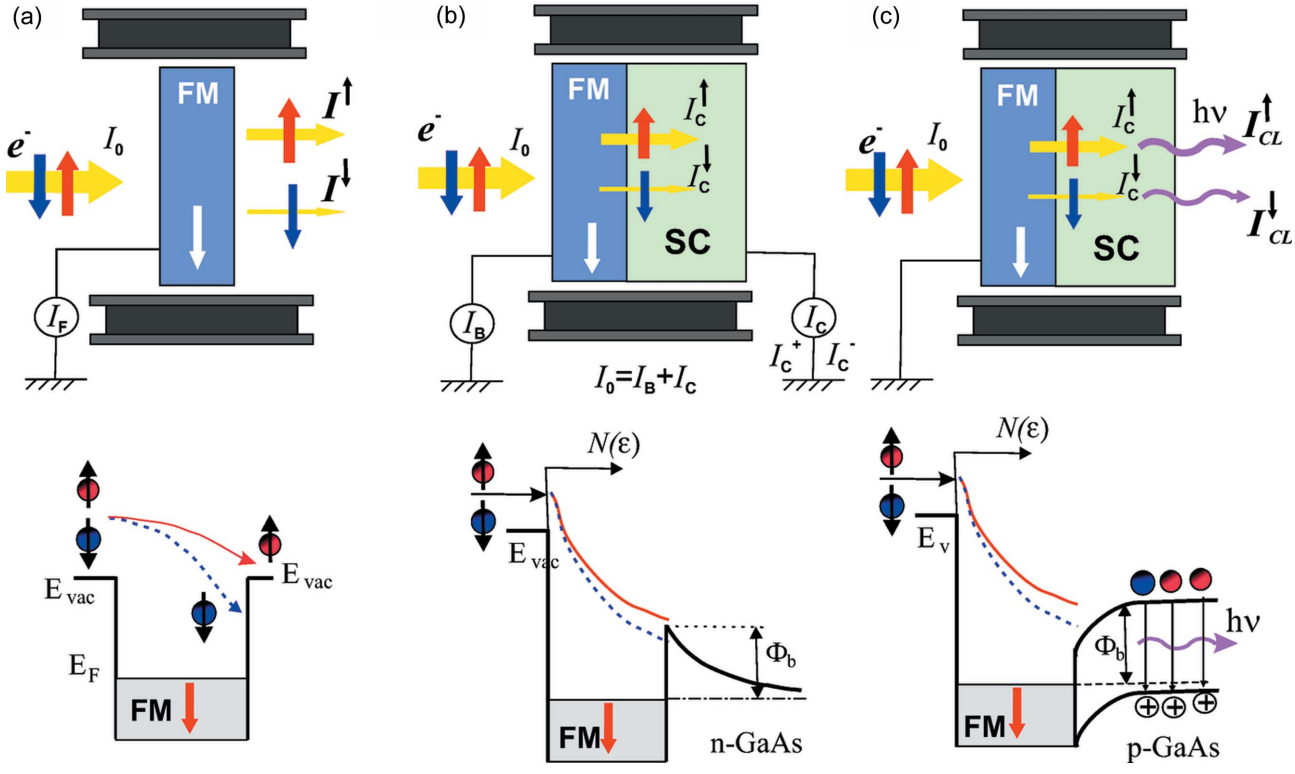

Figure 1
Working principle of spin filter in transmission geometry. (*a*) Ultrathin magnetic film preferentially transmits electrons with a parallel incident spin direction with respect to the magnetization orientation. For a given magnetization, an asymmetry between the transmitted currents $I^{\uparrow}$ and $I^{\downarrow}$ is measured (Oberli *et al.*, 1998; Lassailly *et al.*, 1994). (*b*) Scheme of the three-terminal hybrid device. The emitter provides spin-polarized free electrons. The electrons are injected into the FM-SC junction. Base (FM) and collector (SC) currents are separately detected (Filippe *et al.*, 1998; Tereshchenko *et al.*, 2011). In the magnetic layer, the relaxation is different for majority and minority spin electrons leading to two different distributions $N(\epsilon)$ at the junction. The SHB at the interface plays the selector role for two electron energy distributions. (*c*) By changing the *n*-type to *p*-type semiconductor, optical detection of injected electrons becomes possible (Li *et al.*, 2014). The interface barrier Φ_b in this case is the difference between the conduction band minimum in the bulk and the Fermi level, and also acts as the selector between majority and minority spin-polarized injected electrons.

tion of polarization in the electron beam section and cannot be used in count mode as well.

1.2. Electron spin polarimetry in ferromagnetic/semiconductor hybrid structures: towards optical spin detection with spatial resolution

1.2.1. Detection of an in-plane spin component in the ferromagnetic/semiconductor heterojunction. To overcome the above-mentioned shortcomings, the next step is the optical method, which allows the user to detect cathodoluminescence (CL) in single-photon registration mode. The first reported use of optical electron polarimetry involved the measurement of fluorescent polarization in atomic transitions excited by electrons whose polarization was to be measured (Eminyan & Lampel, 1980). In the solid-state semiconductor target, by changing the *n*-type to *p*-type semiconductor, shown in Figs. 1(*b*) and 1(*c*), optical detection of injected electrons becomes possible. Fig. 1(*c*) demonstrates the principle of optical spin detection. The interface barrier Φ_b in this case is the difference between the conduction band minimum in the semiconductor bulk and the Fermi level, also acting as the selector between majority and minority spin-polarized injected electrons.

The first experimental evidence of spin filtering effects for free electrons in an FM-SC structure by optical detection of CL intensity was demonstrated by Li *et al.* (2014). A magnetic layer, with the in-plane easy magnetization axis, works as a spin filter for incoming electrons with the spin components S_x and S_y parallel to the surface. Electrons transmitted through the metal/semiconductor junction recombine radiatively in the semiconductor structure (quantum wells). Due to the electron spin-filter effect across the FM-SC structure, the CL intensity (I_x, I_y) is found to depend on the relative orientation between the injected electronic spin polarization and the FM layer magnetization. The measured difference in CL light intensity $P_{x,y} = (I_{x,y}{}^{\uparrow} - I_{x,y}{}^{\downarrow})/(I_{x,y}{}^{\uparrow} + I_{x,y}{}^{\downarrow})$ is proportional to the polarization of injected electrons and thus allows the user to determine two spin projections in the plane of the detector. The CL method allows the user to measure all three spin components: two in-plane components using the spin-filter effect in an FM film with in-plane easy axes (Li *et al.*, 2014) and the third (perpendicular to target surface) by measuring CL polarization light from recombined polarized electrons with holes in the semiconductor (Göckel *et al.*, 1990; Alperovich *et al.*, 2005; Golyashov *et al.*, 2020).

1.2.2. Detection of out-of-plane spin components in the ferromagnetic/semiconductor heterojunction. For the incoming electrons with out-of-plane spin polarization through the FM-SC interface, the intensity of circularly polarized CL light can be detected from recombined polarized electrons with holes in the semiconductor. It is known, when the spin polarization vector $\mathbf{P}_0$ of the incident electron beam is chosen to be perpendicular to **M**, it rotates in the direction of **M** and simultaneously also precesses around **M**. This signifies partial depolarization of the electron beam with respect to the P_z component (Fig. 2). Both the spin rotation and precession angles are dependent on the type and thickness of FM and can be taken into account (Weber *et al.*, 2001).

In principle, in order to measure the normal P_z component of electron beam polarization, it is not necessary to use an FM filter. The CL process is the inverse to the photoemission process in which the interaction between the angular momentum of circularly polarized photons and the electron spins in semiconductors results in convenient spin-polarized electron sources (Pierce, 1995). To prepare the spin-polarized electron source, the crystal surface is covered with caesium and oxygen in order to obtain a negative electron affinity which permits the conduction-band spin-polarized electrons to leave the crystal with spin polarization ranging from ∼20%

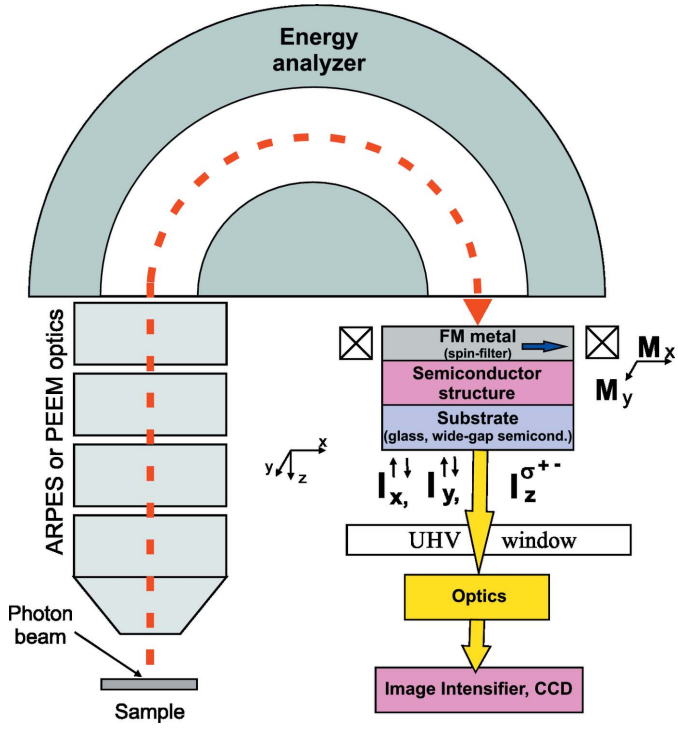

Figure 2
Schematic of the hemispherical detector with an FM-SC spin-filter detector combination. The principle of optical spin detection in a hybrid structure consists of a thin magnetic layer deposited on a semiconductor structure. The magnetic layer has an in-plane easy magnetization axis and works as a spin filter for incoming electrons with the spin components S_x and S_y parallel to the surface. Electrons transmitted through the metal/semiconductor junction recombine radiatively in the SC structure (quantum wells, QDs). Because of the electron spin filtering across the FM-SC structure, the CL intensity (I_x, I_y), collected from the rearside, is found to be dependent on the relative orientation between the injected electronic spin polarization and the FM layer magnetization (Li *et al.*, 2014). The measured difference in light intensity $P_{x,y} = (I_{x,y}{}^{\uparrow} - I_{x,y}{}^{\downarrow})/(I_{x,y}{}^{\uparrow} + I_{x,y}{}^{\downarrow})$ is proportional to the polarization of injected electrons and thus allows the user to determine two spin projections in the plane of the detector. Electrons injected with out-of-plane polarization, transmitted through the FM-SC junction, recombine radiatively in the semiconductor structure with circular polarization, which can be detected by means of polarizing optics (quarter-wave plate and linear polarizer). The measured light polarization degree $P_z = (I_z{}^{\uparrow} - I_z{}^{\downarrow})/(I_z{}^{\uparrow} + I_z{}^{\downarrow})$ is proportional to the polarization of injected electrons and thus allows the user to determine the out-of-plane spin projection of the detector. Combination of the spin detector with optical detectors, such as an image intensifier and/or a CCD camera outside of the vacuum chamber is promising in the realization of multichannel spin detection.

(bulk GaAs) to 90% (semiconductor superstructures). Polarized CL is the reverse process. Selection rules state an asymmetry in the optical transitions in semiconductors when the electrons with different spin projections recombine. Consequently, circularly polarized CL is emitted from a *p*-type semiconductor under injection of spin-polarized electrons. This process was studied earlier in III–V semiconductors with surfaces under the state of positive (Fromme *et al.*, 1989) and negative electron affinity (Göckel *et al.*, 1990; Alperovich *et al.*, 2005). Since the efficiency of the depolarization processes is reduced with decreasing electron energy, it is necessary to lower the work function of the target semiconductor structure in order to achieve low injected electron energy in the conduction band. Electrons, injected with out-of-plane polarization, recombine radiatively in the semiconductor structure with circular light polarization [clockwise (CW) or counterclockwise (CCW)], which can be detected by means of polarizing optics (quarter-wave plate and linear polarizer). The measured light polarization degree $P_{\mathrm{CL}z} = (I_{\sigma+} - I_{\sigma-})/(I_{\sigma+} + I_{\sigma-})$, where $I_{\sigma+}$ ($I_{\sigma-}$) is the intensity of the σ^+ (σ^-) polarized emission component with $\pm$ helicity, is proportional to the polarization of injected electrons and thus allows the spin projection to be determined out-of-plane of the detector (Göckel *et al.*, 1990; Alperovich *et al.*, 2005; Golyashov *et al.*, 2020). This circular polarization P_{CL} is directly related to the electron polarization P_{e} at the instant of recombination by $P_{\mathrm{CL}} = \alpha P_{\mathrm{e}}$, where $P_{\mathrm{e}} = (N^{\uparrow} - N^{\downarrow})/(N^{\uparrow} + N^{\downarrow})$, and $N^{\uparrow}$ and $N^{\downarrow}$ are the densities of electrons with 1/2 spin projection along the direction of light propagation. The coefficient α is equal to $-1/2$ for a cubic bulk III–V semiconductor like GaAs with degenerate heavy-hole and light-hole valence bands. The circular polarization of the CL light reflects the spin-polarization $P_{\mathrm{e}} = \beta P_0$ of the recombining electrons, where β is the depolarization factor studied in detail as a function of injected electron energy from spectral CL measurements (Golyashov *et al.*, 2020). An asymmetry measured in the optical experiment for known electron beam polarization $A = P_{\mathrm{CL}}/P_0 = \alpha\beta = S$ is the Sherman function for optical detection of the incident electron polarization. One can see that S can reach the maximum value equal to α in the case of absence of spin depolarization, *i.e.* $\beta = 1$. This condition can be realized if electrons are injected directly at the bottom of the conduction band and if they recombine so fast that no spin relaxation occurs before recombination. On the other hand, reducing the lifetime of injected electrons results in a decrease of detected CL intensity. To minimize the accumulation time (maximize signal-to-noise ratio), it is necessary to optimize the value $F = S^2 N_{\mathrm{ph}}/N_{\mathrm{e}}$, where the ratio $N_{\mathrm{ph}}/N_{\mathrm{e}}$ reflects the CL yield (number of outcoming photons/number of injected electrons).

The formula $F_{\mathrm{single}} = S^2 N_{\mathrm{ph}}/N_{\mathrm{e}}$ reflects the efficiency of the single-channel mode detector. In order to improve the detection efficiency, multichannel spin detection is desirable by measuring more than one data point at the same time (Fig. 2). In the semiconductor structure, in-plane CL detection allows the user to resolve the intensity and polarization of CL from injected spin-polarized electrons with spatial resolution. Theoretically, the limiting spatial resolution that can be achieved with a semiconductor detector resolution is determined by the minority charge and spin diffusion lengths. The charge diffusion length, which is 3–5 µm for *p*-GaAs, limits the spatial resolution of CL detection, while the spin diffusion length is about 0.5 µm and allows even better spatial resolution. This estimation shows the possibility to achieve at least $10^3 \times 10^3 = 10^6$ channels for the 10 mm × 10 mm imaging region.

2. Model system for an image-type spin detector

2.1. Experiment: spectral and spatial CL measurements

We developed an image-type spin detector prototype for measuring the normal (to the surface of the detector) component of the electron beam polarization, utilizing the injection of spin-polarized free electrons in a heterostructure with quantum wells (QWs) and recording the circularly polarized CL with spatial resolution. A flat vacuum photodiode composed of two effective NEA semiconductor electrodes was designed and studied (Rodionov *et al.*, 2017; Tereshchenko *et al.*, 2017; Golyashov *et al.*, 2020). Schematic presentation of the compact vacuum photodiode with photographs of the device from the photocathode side and the target (anode) and operation principle for the investigation of spin-dependent injection are shown in Figs. 3(*a*), 3(*b*) and 3(*c*). A GaAs photocathode was used as a source of spin-polarized electrons and the anode, an A^3B^5 heterostructure with QWs, as the spin detector. This system enables the user to determine the energy distribution of the emitted conduction electrons (Tereshchenko *et al.*, 2017).

The photocathode consists of an active 2.5 µm GaAs layer and the $Al_{0.6}Ga_{0.4}As$ layer with SiO antireflection coating, through which the structure is bonded to the glass of the input window. The semiconductor anode (target) comprises an upper 10 nm GaAs layer, an $Al_{1-x}Ga_xAs$ subsurface layer with a total thickness of 15 nm (5 nm $x = 0.7$, 5 nm $x = 0.4$, and 5 nm $x = 0.7$), three GaAs QWs with a width of 2.0 nm (7 ML) separated by 20 nm $Al_{0.3}Ga_{0.7}As$ barriers, and the last 100 nm $Al_{0.6}Ga_{0.4}As$ bottom layer with SiO antireflection coating. The concentrations of acceptor doping in the cathode and anode were 6×10^{18} cm^{-3} and 3×10^{17} cm^{-3}, respectively. The final step of the cleaning procedure for both the cathode and the anode was carried out inside a glove box flooded with pure nitrogen, in which the cathode and anode were chemically treated in a solution of HCl in isopropanol (Tereshchenko *et al.*, 1999). Both cleaned surfaces are activated to the NEA state by coadsorption of caesium and oxygen (Pakhnevich *et al.*, 2004; Tereshchenko *et al.*, 2004). The photocathode and anode were plane-parallel mounted in an air-tight manner on the opposite flat sides of a cylindrical aluminium oxide body. The diameters of the cathode and anode were 18 mm with a 1.6 mm gap between the electrodes.

The main feature of the vacuum photodiode created is that both electrodes are semiconductor heterostructures with close work functions, and the vacuum levels of both electrodes are below the conduction-band minimum in the bulk, being in the

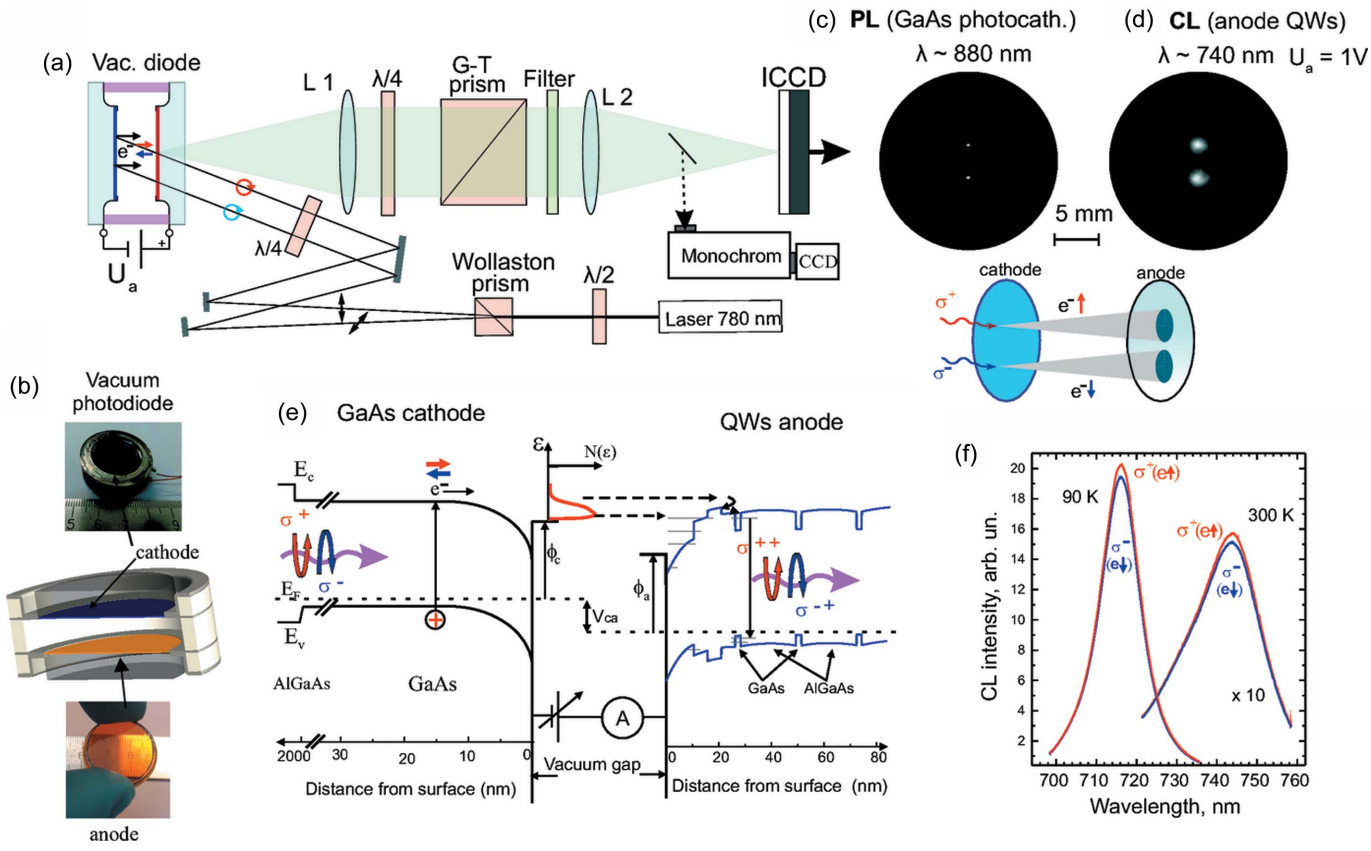

Figure 3
Experimental setup. (*a*) Schematic drawing of optical setup for spatial CL polarization detection. (*b*) Vacuum photodiode for spin polarization measurements. Upper photograph shows the assembled photodiode from the GaAs photocathode side. Schematic drawing of the vacuum photodiode in the cross section and a photograph of the anode QW structure are shown below. Electrons photoemitted under the $h\nu$ photon excitation from the GaAs source are injected in the heterostructure target with QWs. (*c*) Image of photoluminescence intensity distribution in the GaAs photocathode. (*d*) Image of CL intensity distribution in the anode QW structure under injection of 1 eV electrons emitted from the photocathode at room temperature. (*e*) Energy diagram of both the GaAs source and the QW target with the NEA separated by a vacuum gap. E_c is the conduction band, E_v is the valence band and E_F is the Fermi level. The GaAs cathode is a source of spin-polarized electrons and the heterostructure with QWs is the detector. (*f*) Circularly polarized (σ^+, σ^-) components of the CL spectra excited by the injection of spin polarized electrons emitted from the cathode at an accelerating voltage of 0.5 V and T = 300 K and 90 K.

so-called negative-electron-affinity state shown in the band diagram of two electrically connected semiconductor electrodes [Fig. 3(*e*)] (Rodionov *et al.*, 2017).

The experimental scheme of polarized electron detection is shown in Fig. 3(*a*). The GaAs photocathode is optically pumped by a diode laser ($h\nu$ = 1.59 eV). In order to simultaneously create two electron beams with opposite spin polarizations, we used a Wollaston prism. It splits the laser beam in two with orthogonal linear polarizations. Since the laser light is linearly polarized, the intensity ratio of these two beams can be adjusted to 1:1 by rotating a half-wave plate. Then the beams are passed through a single quarter-wave plate to convert their horizontal and vertical linear polarizations into clockwise (CW, right) and counterclockwise (CCW, left) circular, and are directed on the (001) surface of the photocathode through the photodiode anode window, thus operating in reflection mode. The photoelectrons excited by circularly polarized light in GaAs are spin-polarized due to the spin–orbit coupling and selection rules (Meier & Zakharchenya, 1984). The 1.59 eV photon energy is lower than the spin–orbit split band in GaAs at room- and low-temperatures and, as a result, 50% polarization of photoexcited electrons along the direction of light propagation can be expected. The emitted electrons are longitudinally polarized along the normal to the detector surface, and their polarization state (spin up or spin down) is dependent on the direction of the photon circular polarization (CW or CCW). The sign of laser beam circular polarization, and thus the sign of electron beam spin polarization, can be changed by rotating the quarter-wave plate by 90°. The instability of the photoemission current from the photocathode was mainly determined by the excitation laser intensity ripple and was maintained within 0.1%.

Photoluminescence (PL) emitted from the GaAs photocathode under radiative recombination of photoexcited electrons and CL from the anode under electron injection were collected through the anode window of the vacuum photodiode and projected on a cryogenically cooled lens coupled image intensifier CCD (ICCD) detector for image recording [Figs. 3(*c*) and 3(*d*)] or a monochromator input slit for spectral detection [Fig. 3(*f*)] using simple image transfer optics. The emission spectra were recorded using a 0.3 m monochromator equipped with a thermoelectrically cooled CCD detector.

Interference filters were used to select the appropriate spectral region during image recording of PL or CL. The circular polarizations of both PL and CL were analyzed by a polarimeter consisting of an achromatic quarter-wave plate and a Glan–Taylor prism. The spin polarization of the electrons injected in the heterostructure was measured according to the degree of CL circular polarization. The circular polarization degree of CL: is determined as $P_{CLz} = (I_{\sigma+} - I_{\sigma})/(I_{\sigma+} + I_{\sigma-})$, where $I_{\sigma+}$ ($I_{\sigma-}$) is the intensity of the σ^+ (σ^-)-polarized CL emission components with $\pm$ helicity, respectively. For the elimination of instrumental asymmetries, we reversed the electron polarization at the GaAs-photocathode source, simply by reversing the sign of the circular polarization of the exciting light. An additional check is provided by analyzing the CL polarization by a quarter-wave plate tuned to the target QWs optical transition (*i.e.* 712 nm and 742 nm at 77 K and 300 K, respectively) and a linear polarizer. From these measurements, the value of the instrumental asymmetries was found to be less than 0.2%. The change in circular polarization sign of laser light excitation from $\sigma+$ to $\sigma-$ reverses the sign of CL polarization.

2.2. Detection of spin polarization in image-type mode

To characterize the target properties, we started with integral characteristics such as the dependence of the CL intensity and its spectral polarization on the energy of the injected spin-polarized electrons, shown in Figs. 4(*a*) and 4(*b*). The CL spectra recorded at different accelerating voltages at room temperature show a peak with an energy of 1.67 eV (742 nm) [Fig. 4(*a*)], which is in good agreement with the calculated energy band diagram of quantum levels in GaAs/AlGaAs QWs, shown in Fig. 3(*e*). The CL signal is recordable at the minimum accelerating voltage of 0.5 V at room temperature. The intensity rapidly increases by several orders of magnitude starting from 0.5 eV to 1 eV, caused by electron injection into the semiconductor bulk and their subsequent radiative recombination. The absence of the signal at lower voltages is associated with the fact that the injected electron energy is insufficient to overcome the surface barrier and enter the $Al_xGa_{1-x}As$ conduction band (Golyashov *et al.*, 2020). As a result, the majority of the electrons are reflected from the barrier and nonradiatively recombine at the anode surface. The dependence of the integrated nonpolarized CL on the energy of the electrons (0.5–2.5 eV) injected into the heterostructure with QWs is shown in Fig. 5(*b*).

By the next step, we detect the circularly polarized components of the CL emission excited by the spin-polarized electron injection in the heterostructure with QWs. The CL spectra measured in $\sigma^+(\sigma^-)$ polarizations during the injection of electrons with 0.5 eV energy and temperatures of 300 K are shown in Fig. 4(*b*). The circular polarization degree P_{CL} of the CL emission is shown in Fig. 4(*c*). It is evident that the maximum degree of polarization is attained in the low photon energy region of the CL spectrum, which is prevalently formed by electron transitions (recombination) to the heavy-hole subband (Golyashov *et al.*, 2020). As for the higher photon energy region of the spectrum, the CL signal is the sum of electron optical transitions to the heavy- and light-hole regions, thereby leading to a decrease in the degree of CL polarization. The maximum detected CL polarization in the studied QW structures was 2% by the injection of 20% spin-polarized electron beam, meaning asymmetry is equal to $S = A_{CL}/P_0 = 0.1$.

To demonstrate the ability of the semiconductor target to detect spatial spin polarization, two electron beams with

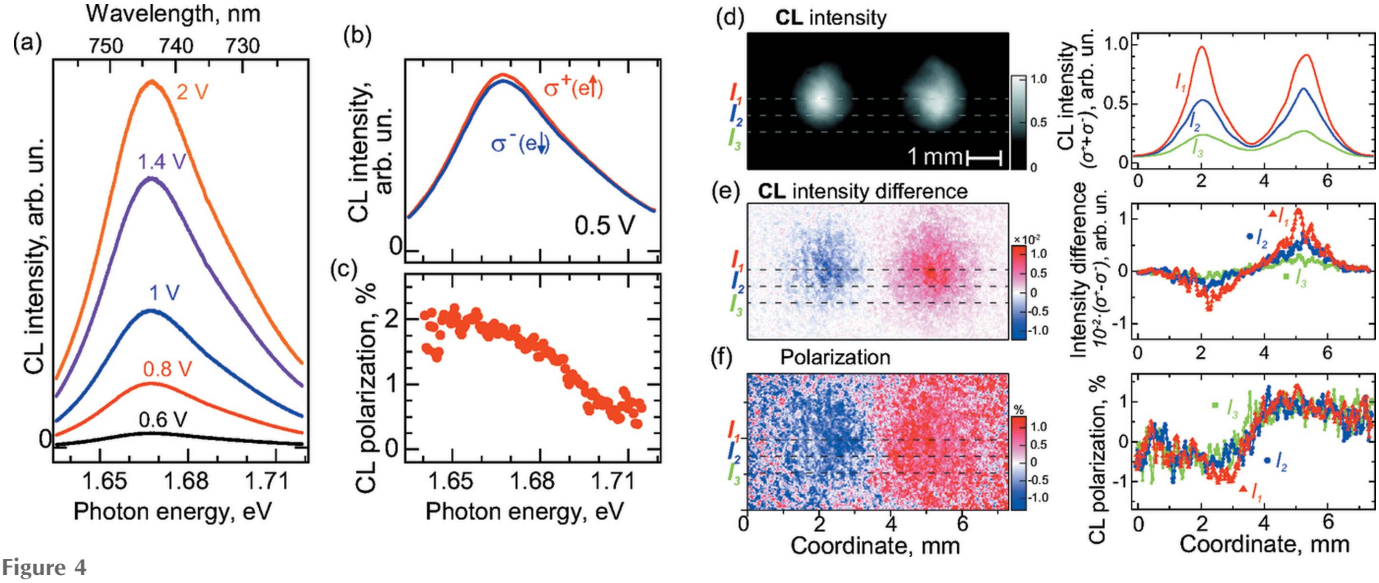

Figure 4
(*a*) CL spectra measured at various accelerating bias. (*b*) Circularly polarized (σ^+, σ^-) components of the CL spectra excited by the injection of the electrons with opposite spin polarizations at an accelerating voltage of 0.5 V and T = 300 K. (*c*) Degree of circular polarization of the CL emission at different temperatures. (*d*) Image of spin-integrated CL intensity, (*e*) difference of CL intensity between 'spin-up' and 'spin-down' ($I_z^{\uparrow} - I_z^{\downarrow}$), and (*f*) derived CL circular polarization degree 2D distribution $P_z = (I_z^{\uparrow} - I_z^{\downarrow})/(I_z^{\uparrow} + I_z^{\downarrow})$ with the corresponding horizontal profiles marked lines l_1, l_2 and l_3. The images were taken at an accelerating voltage of 1 V and T = 300 K. The right parts demonstrate intensity (l_i) cross-sections along the coordinates.

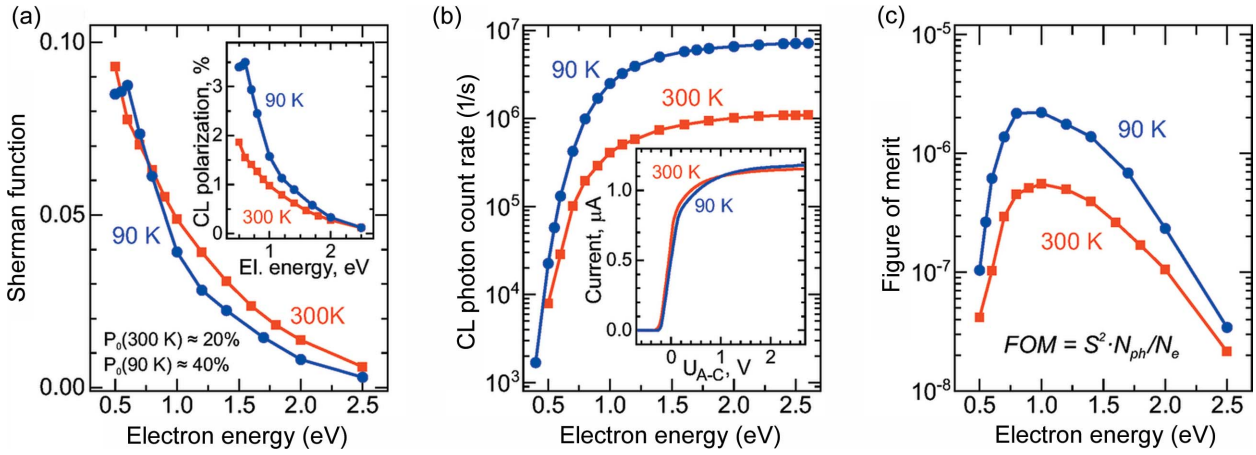

Figure 5
(*a*) Sherman function $S = A_{CL}/P_0$ calculated from CL asymmetry, shown in the insert: dependence of the degree of CL polarization (spin asymmetry A_{CL}) on the energy of injected electrons at $T = 300$ K (red squares) and $T = 90$ K (blue circles). (*b*) Dependence of the integrated nonpolarized CL intensity (logarithmic scale) on the energy of the electrons injected into the $Al_xGa_{1-x}As/GaAs/Al_xGa_{1-x}As$ heterostructure with QWs. The insert shows the photocurrents as a function of applied bias. (*c*) Resulting efficiency $F = S^2N_{ph}/N_{el}$ as a function of the injecting electron energy, where N_{ph} is the emitted photon number and N_{el} is the incident electron number (number of outcoming photons per incident electron). The energy of the injected electrons is proportional to the bias between the anode and cathode, and the elementary charge of the electron.

opposite polarization were simultaneously injected into the detector from GaAs photocathode [Figs. 4(*d*), 4(*e*) and 4(*f*)]. By forming a negative electron affinity on the (001) GaAs surface, spin-polarized electrons in conduction bands are emitted into a vacuum and measured using a semiconductor heterostructure via CL detection. The spot size of CL images is determined by the angular distribution of electrons emitted from the GaAs photocathode and shown schematically in Figs. 3(*c*) and 3(*d*). Fig. 4(*d*) shows the image of spin-integrated CL intensity from two spots induced by two opposite spin-polarized electron beams injected into the tested target. The images were taken at an accelerating voltage of 1 V and $T = 300$ K and reflect the electron distribution in the cross-section. In this case, the CL polarization in the cross section of two electron beams should have the opposite sign and be determined by the polarization of photoemitted electrons exited by absorbed circularly polarized light in the photocathode.

Fig. 4(*e*) shows the CL intensity difference $(I_z^{\uparrow} - I_z^{\downarrow})$. Due to the injection of opposite polarized electron beams and its recombination in QWs, the emitted CL contains both polarized emission components σ^+ (σ^-) with $\pm$ helicity oppositely distributed intensity in two spots: spin up $I_z^{\uparrow}$ and spin down $I_z^{\downarrow}$, respectively. To determine the CL polarization asymmetry and to exclude experimental asymmetry induced by imperfection of optical elements and their position, four CL pictures are registered by changing the electron spin polarization (with a fixed optical analyzer) and analyzer (with fixed electron polarization) by rotation of the quarter-wave plate. In fact, the difference in asymmetry between these two measurements did not exceed 0.1%, meaning good optical alignment. The CL polarization asymmetry image $P_z = (I_z^{\uparrow} - I_z^{\downarrow})/(I_z^{\uparrow} + I_z^{\downarrow})$ is shown in Fig. 4(*f*). The detected asymmetry at 1 eV electron injection energy is 1%, which is in good agreement with spectral measurements [Fig. 4(*a*)].

2.3. Spin detector characteristics

For spin-polarimetry applications, the important characteristics are the Sherman function $S = A_{CL}/P_0$ (defined as the detected spin asymmetry for a 100%-polarized electron beam), which, in our case, expresses the spin selectivity of the heterostructure, and the FOM $F = S^2N_{ph}/N_{el}$, which defines the polarimeter sensitivity, where N_{ph}/N_{el} in the case of optical detection is the number of outcoming photons per incident electron. To assess the maximum achievable degree of CL circular polarization in our structures, the dependence of CL circular polarization on the energy of injected electrons in the range 0.4–2.5 eV was measured [Fig. 5(*a*) insert] for temperatures of 300 K and 90 K. The degree of CL polarization in the region of low kinetic energies, 0.4–0.65 eV, reached its maximum value of 2.0% at 300 K and 3.5% at 90 K and it monotonically decreases to less than 0.1% (determined by the measurement accuracy) for both temperatures as the electron energy increases up to 2.5 eV. The dependences of the Sherman functions $S = A_{CL}/P_0$ on the injected electron energy are shown in Fig. 5(*a*), where A_{CL} is the measured value of the degree of CL polarization [Fig. 5(*a*) insert] and P_0 is the degree of incident electron beam polarization. Considering that the average degree of polarization of an electron beam is 20% ($T = 300$ K) and 35–40% ($T = 90$ K) (Golyashov *et al.*, 2020), the asymmetry in detection of the CL polarization degree reaches a maximum $S = 0.1$ at a minimal injection energy of 0.5 eV for both temperatures. As is evident from Fig. 5(*a*), the degree of CL polarization at low temperature in the energy range 0.45–0.65 eV is independent of the energy of the injected electrons, which is presumably associated with a direct tunneling of spin-polarized electrons from vacuum to the QW closest to the surface. The variation of the spin asymmetry with the injection energy is dependent on the spin-relaxation mechanism in the heterostructure matrix

($Al_xGa_{1-x}As$), studied for the target used by Golyashov *et al.* (2020). The theoretical estimate for the maximum asymmetry value was 0.5, whereas the measured value amounted to 0.1 and is almost independent of temperature. Assuming that spin does not scatter at the interface and over the distance to the first QW when electrons are injected directly to the conduction band minimum, it is likely that the residual electron polarization is determined by the spin scattering (depolarization) in QWs. This means that the electron scattering in the QW anode structure is a main contributor to the electron spin depolarization.

Another important parameter is the detection efficiency (intensity response) N_{ph}/N_{el}. The fundamental difference between the method presented and existing ones is the principle of detection. In detectors based on the spin-exchange interaction (VLEED) and SOI (Mott), the ratio N/N_0 determines the efficiency of electron detection, where N_0 is the number of incoming electrons and N is the number of detected electrons. In our case, we measured the intensity and polarization of CL, in other words, transformation of electrons into photons; and in this case, we determined the detection efficiency as N_{ph}/N_{el}, where N_{ph} is the outcoming photon number and N_{el} is the number of injected electrons. Thus, the ratio of N_{ph}/N_{el} is an analog of the reflectivity $R = I/I_0$ in scattering Mott-, VLEED- and SPLEED-type detectors and characterizes the detection efficiency of the semiconductor target. This detection efficiency is equivalent to the emission efficiency, which is consistent in the internal and external quantum efficiencies, similar to those routinely used in LED characteristics.

The CL intensity as a function of energy of electron beam injected into the AlGaAs/GaAs heterostructure is shown in Fig. 5(*b*). At room temperature, the CL signal starts to rise around 0.5 V when electron energy is sufficient to overcome the target surface barrier and enter into the conduction band of the AlGaAs matrix and finally become trapped by a QW. The photocurrent is close to saturation at 0.5 V [Fig. 5(*b*) insert], whereas the CL signal continues to increase with electron energy. The CL intensity rapidly increases from 0.5 V to 1 V, which can be attributed to the electron injection into the semiconductor bulk and their subsequent radiative recombination. At low temperatures, CL emission efficiency is almost one order of magnitude higher than at room temperature due to the higher thermalization rate, capturing in QWs and recombination rate. To correctly estimate the ratio N_{ph}/N_{el}, we considered the aspect ratio of the optical scheme and calibrated the detection efficiency of the ICCD system. As a result, we found a rather low value of internal quantum efficiency $N_{ph}/N_{el} \simeq 10^{-4}$.

The resulting single-channel FOM $F = S^2N_{ph}/N_{el}$ is shown in Fig. 5(*c*) as a function of the injected electron energy, where N_{ph}/N_{el} is the number of outcoming photons per incident electron. It increases in the range 0.5–0.8 eV due to the increase in outcoming photons, and decreases with increasing energy above 1.5 eV caused by a decrease in S. The highest and weakly energy-dependent FOM is obtained for the 0.8–1.5 eV kinetic energy range. The FOM is found to be temperature dependent and the maximal values are equal to 5×10^{-7} at 300 K and 3×10^{-6} at 90 K.

2.4. Spin-integrated image mode: amplification and spatial resolution

In Fig. 6, the total CL signal at 742 nm as a function of electron energy in the range 1–1300 eV is plotted. When the voltage increases to 1.5 V [Fig. 5(*b*)], the majority of the electrons enter into the anode bulk and intensity growth slows down. There is a subsequent rise in the CL curve above 3.6 eV (Golyashov *et al.*, 2020), which coincides with the onset of electron–hole pair creation by impact ionization, while the incident current remains constant. During this process, the primary electron excites an additional secondary electron into the conduction band. Then both electrons recombine with the emission of two photons. The CL signal strongly increases, over three orders of magnitude, when the injection energy is increased up to 1 keV. This variation is quite similar to that of the transmitted electron current measured in highly rectifying Pd/Fe/*n*-GaAs junctions (Tereshchenko *et al.*, 2011). Electrons entering the target efficiently can relax their energy and momentum by generating a secondary electron cascade.

The spin-integrated image mode allowed us to test spatial resolution using the standard 1951 USAF test chart in the CL image (Fig. 6 insert). The image was detected at 1 keV electron energy injection by detection using a standard CCD camera (without an image intensifier). We can see many dark horizontal lines and fewer vertical ones. These lines are dislocations produced in some cases (not very successfully) during GaAs and glass bonding and/or a vacuum photodiode assembly process. These dislocations make it difficult to determine the maximum resolution in the studied structure. However, the distance that can be resolved between disloca-

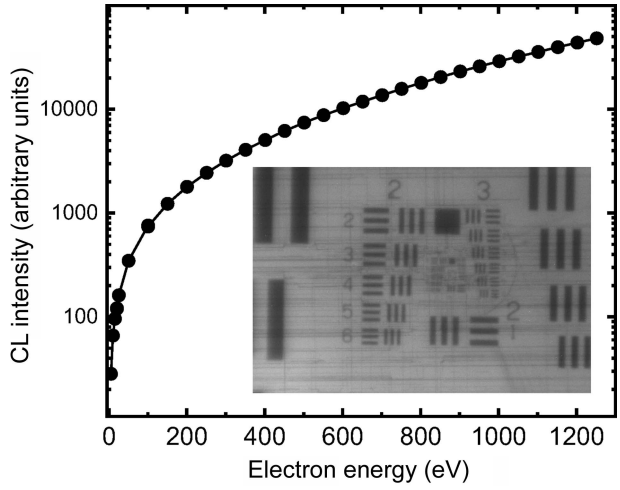

Figure 6
Spin-integrated CL intensity (logarithmic scale) as a function of the energy of the electrons injected into the AlGaAs/GaAs heterostructure measured at 300 K. Insert shows the spin-integrated CL image of the 1951 USAF test chart at the output of the photodiode. These results show that the SC plate is capable of resolving 50-line pairs per millimetre and higher.

tions is less than 10 μm. The presence of dislocations can be the reason for the low internal quantum efficiency of radiative recombination since dislocations are nonradiative recombination centers. The working area of the studied target is 6 cm^2. With a 10 μm × 10 μm spatial resolution of the single channel, more than 10^6 channels can be received.

3. Perspectives

Further theoretical and experimental studies might be worthwhile to find higher asymmetry and internal efficiency than those that we have observed in this first study. A spin detector has to be constructed in such a way that the Sherman function and the intensity response N_{ph}/N_{el} are as large as possible in order to minimize the counting time t that is needed to remain under a given statistical error. In the present experiment, the Sherman function is only 0.1 because of the strong spin depolarization in QWs (Golyashov *et al.*, 2020), but a better tailored heterostructure would increase the spin depolarization factor β towards unity. The highest losses of spin polarization occur during the spin depolarization in a thin QW. An increase in the detection asymmetry efficiency requires an increase in the spin relaxation time τ_s that can be achieved through increasing the thickness of QWs (Malinowski *et al.*, 2000) and decreasing the recombination time τ_r through increasing the doping level of QWs (Meier & Zakharchenya, 1984; Niemeyer *et al.*, 2019). Comparison with PL polarization in the GaAs photocathode shows that the Sherman function can be increased 3–5 times, gaining one order of magnitude in detector efficiency.

The main disadvantage of the target under study is its very low internal efficiency on the order of 10^{-4} photons/electrons. It means that most of the injected electrons recombine with holes nonradiatively. The main source of nonradiative recombination is the open surface, which is crossed by electrons. Due to energy relaxation of the injected electrons in the band-bending region of the target, most of the electrons are trapped by the surface states and, as a result, nonradiatively recombine. The next step will be to overcome this problem by surface barrier engineering and surface passivation (Tereshchenko *et al.*, 2015). Another source of nonradiative recombination is dislocations (Fig. 6), which can reduce the emission process by at least by one order of magnitude. This problem can be eliminated by a proper bonding process between semiconductor and glass or by using a wider gap substrate.

The maximal ratio N_{ph}/N_{el} can be improved drastically by the methods used in the LED technology and evaluated from the external efficiencies of doped GaAs crystals or AlGaAs/GaAs/AlGaAs heterostructures, which are normally light emitters with an internal efficiency up to 100% and external efficiency up to 70% (Schnitzer *et al.*, 1993). This estimate provides hope for obtaining an efficiency several orders of magnitude higher than in this first experiment. Therefore, the single-channel FOM value can be comparable and even higher than a single-channel Mott detector, *i.e.* in the range 10^{-3}–10^{-4}. Note that the efficiency of the optical electron polarimeter based on the measurement of fluorescent polarization in atomic transitions excited by the electrons was estimated to be on the order 10^{-10} (Trantham *et al.*, 1996) with further improvement to 10^{-8} (Pirbhai *et al.*, 2013).

Note that the experiment used for detection of spatial CL polarization suggests an increase in the detection efficiency by a factor of 10^6 and higher compared with a single-channel detector. A spin detector based on an FM-SC structure might replace the conventional microchannel plate (MCP)-screen electron detector in standard high-resolution low-energy electron spectrometers.

4. Conclusions

We have presented a concept of the image-type FM-SC electron spin detector and demonstrated the feasibility of semiconductor electrodes in detecting the degree of free-electron spin polarization in multichannel mode using the polarized CL technique. This polarimeter offers several attractive features for electron spin analysis. It is relatively simple in its construction and is compact. Despite a relatively low efficiency of 10^{-6}–10^{-7} demonstrated in single-channel mode, the multichannel approach counteracts the small inherent efficiency of the conversion by a factor of 10^4–10^6. We have worked on the heterostructure design of the effective optical spin polarimeter, which allows the incoming polarized electrons to effectively transfer to the outcoming photons, with a Sherman function of 0.3–0.5 and electron-to-photon external conversion efficiency on the order of 10^{-2}–10^{-3} photons/electrons. These parameters will make it possible to achieve single-channel FOM on the order of 10^{-3}–10^{-4}. The next step will be taken towards the creation and optimization of the FM-SC structures for an imaging-type 3D spin-resolving electron detector. The detector can be fitted to a standard electron analyzer instead of an MCP to yield a spin-resolved image in the energy and angle coordinates, or a momentum microscope to yield an image in the momentum coordinates at a fixed energy. The CL mapping can be performed in photon counting mode to record the distribution of electrons according to the momentum, energy and three spin components, *i.e.* to obtain extensive information about the dispersion law.

Funding information

Funding for this research was provided by: Ministry of Education (grant No. 075-15-2020-797 (13.1902.21.0024).

References

Alperovich, V. L., Terekhov, A. S., Jaroshevich, A. S., Lampel, G., Lassailly, Y., Peretti, J., Rougemaille, N. & Wirth, T. (2005). *Nucl. Instrum. Methods Phys. Res. A*, **536**, 302–307.

Bertacco, R., Onofrio, D. & Ciccacci, F. (1999). *Rev. Sci. Instrum.* **70**, 3572–3576.

Bigi, C., Das, P. K., Benedetti, D., Salvador, F., Krizmancic, D., Sergo, R., Martin, A., Panaccione, G., Rossi, G., Fujii, J. & Vobornik, I. (2017). *J. Synchrotron Rad.* **24**, 750–756.

Drouhin, H. J., van der Sluijs, A. M., Lassailly, Y. & Lampel, G. (1996). *J. Appl. Phys.* **79**, 4734.

Eminyan, M. & Lampel, G. (1980). *Phys. Rev. Lett.* **45**, 1171–1174.

Erbudak, M. & Müller, N. (1981). *Appl. Phys. Lett.* **38**, 575–577.

Escher, M., Weber, N. B., Merkel, M., Plucinski, L. & Schneider, C. M. (2011). *e-J. Surf. Sci. Nanotech.* **9**, 340–343.

Filippe, A., Drouhin, H.-J., Lampel, G., Lassailly, Y., Nagle, J., Peretti, J., Safarov, V. I. & Schuhl, A. (1998). *Phys. Rev. Lett.* **80**, 2425.

Fromme, B., Baum, G., Göckel, D. & Raith, W. (1989). *Phys. Rev. B*, **40**, 12312–12318.

Gay, T. J. (2009). *Adv. At. Mol. Opt. Phys.* **57**, 157.

Ghiringhelli, G., Larsson, K. & Brookes, N. B. (1999). *Rev. Sci. Instrum.* **70**, 4225–4230.

Göckel, D., Baum, G., Fromme, B., Lehmann, V., Lohmann, B. & Raith, W. (1990). *Phys. Rev. B*, **42**, 7242–7244.

Golyashov, V. A., Rusetsky, V. S., Shamirzaev, T. S., Dmitriev, D. V., Kislykh, N. V., Mironov, A. V., Aksenov, V. V. & Tereshchenko, O. E. (2020). *Ultramicroscopy*, **218**, 113076.

Hillebrecht, F. U., Jungblut, R. M., Wiebusch, L., Roth, C., Rose, H. B., Knabben, D., Bethke, C., Weber, N. B., Manderla, S., Rosowski, U. & Kisker, E. (2002). *Rev. Sci. Instrum.* **73**, 1229–1234.

Hoesch, M., Greber, T., Petrov, V. N., Muntwiler, M., Hengsberger, M., Auwärter, W. & Osterwalder, J. (2002). *J. Electron Spectrosc. Relat. Phenom.* **124**, 263–279.

Ji, F., Shi, T., Ye, M., Wan, W., Liu, Z., Wang, J., Xu, T. & Qiao, S. (2016). *Phys. Rev. Lett.* **116**, 177601.

Jozwiak, C., Graf, J., Lebedev, G., Andresen, N., Schmid, A. K., Fedorov, A. V., El Gabaly, F., Wan, W., Lanzara, A. & Hussain, Z. (2010). *Rev. Sci. Instrum.* **81**, 053904.

Kirschner, J. (1985). *Polarized Electrons at Surfaces*. Berlin: Springer-Verlag.

Kirschner, J. (2020). Private communication.

Kirschner, J. & Feder, R. (1979). *Phys. Rev. Lett.* **42**, 1008–1011.

Kirschner, J., Giebels, F., Gollisch, H. & Feder, R. (2013). *Phys. Rev. B*, **88**, 125419.

Kisker, E., Clauberg, R. & Gudat, W. (1982). *Rev. Sci. Instrum.* **53**, 1137–1144.

Kolbe, M., Lushchyk, P., Petereit, B., Elmers, H., Schönhense, G., Oelsner, A., Tusche, C. & Kirschner, J. (2011). *Phys. Rev. Lett.* **107**, 207601.

Kozina, X., Ikenaga, E., Viol Barbosa, C. E., Ouardi, S., Karel, J., Yamamoto, M., Kobayashi, K., Elmers, H. J., Schönhense, G. & Felser, C. (2016). *J. Electron Spectrosc. Relat. Phenom.* **211**, 12–18.

Kutnyakhov, D., Lushchyk, P., Fognini, A., Perriard, D., Kolbe, M., Medjanik, K., Fedchenko, E., Nepijko, S. A., Elmers, H. J., Salvatella, G., Stieger, C., Gort, R., Bähler, T., Michlmayer, T., Acremann, Y., Vaterlaus, A., Giebels, F., Gollisch, H., Feder, R., Tusche, C., Krasyuk, A., Kirschner, J. & Schönhense, G. (2013). *Ultramicroscopy*, **130**, 63–69.

Lassailly, Y., Drouhin, H.-J., van der Sluijs, J., Lampel, G. & Marliere, C. (1994). *Phys. Rev. B*, **50**, 13054.

Li, X., Tereshchenko, O. E., Majee, S., Lampel, G., Lassailly, Y., Paget, D. & Peretti, J. (2014). *Appl. Phys. Lett.* **105**, 052402.

Maaß, H., Bentmann, H., Seibel, C., Tusche, C., Eremeev, S. V., Peixoto, T. R. F., Tereshchenko, O. E., Kokh, K. A., Chulkov, E. V., Kirschner, J. & Reinert, F. (2016). *Nat. Commun.* **7**, 11621.

Malinowski, A., Britton, R. S., Grevatt, T., Harley, R. T., Ritchie, D. A. & Simmons, M. Y. (2000). *Phys. Rev. B*, **62**, 13034–13039.

Medjanik, K., Fedchenko, O., Chernov, S., Kutnyakhov, D., Ellguth, M., Oelsner, A., Schönhense, B., Peixoto, T. R. F., Lutz, P., Min, C.-H., Reinert, F., Däster, S., Acremann, Y., Viefhaus, J., Wurth, W., Elmers, H. J. & Schönhense, G. (2017). *Nat. Mater.* **16**, 615–621.

Meier, F. & Zakharchenya, B. (1984). *Optical Orientation*. North Holland: Elsevier.

Mott, N. F. (1929). *Proc. R. Soc. London Ser. A*, **124**, 425.

Niemeyer, M., Kleinschmidt, P., Walker, A. W., Mundt, L. E., Timm, C., Lang, R., Hannappel, T. & Lackner, D. (2019). *AIP Adv.* **9**, 045034.

Oberli, D., Burgermeister, R., Riesen, S., Weber, W. & Siegmann, H. C. (1998). *Phys. Rev. Lett.* **8**, 4228–4231.

Okuda, T., Takeichi, Y., Maeda, Y., Harasawa, A., Matsuda, I., Kinoshita, T. & Kakizaki, A. (2008). *Rev. Sci. Instrum.* **79**, 123117.

Pakhnevich, A. A., Yazkov, A. V., Bakin, V. V., Tereshchenko, O. E., Scheibler, H. E., Jaroshevich, A. S., Kosolobov, S. N. & Terekhov, A. S. (2004). *Proceedings of the 16th International Spin Physics Symposium and Workshop on Polarized Electron Sources and Polarimeters*, 10–16 October 2004, Trieste, Italy, p. 959. World Scientific Publishing.

Pappas, D. P., Kämper, K.-P., Miller, B. P., Hopster, H., Fowler, D. E., Brundle, C. R., Luntz, A. C. & Shen, Z.-X. (1991). *Phys. Rev. Lett.* **66**, 504–507.

Petrov, V. N., Gabdullin, P. G., Pavlov, A. V., Ustinov, A. B., Strokov, V. N. & Dill, H. (2020). *Proceedings of the XXV International Symposium on Nanophysics and Nanoelectronics*, 9–12 March 2020. Nizhny Novgorod.

Petrov, V. N., Grebenshikov, V. V., Andronov, A. N., Gabdullin, P. G. & Maslevtcov, A. V. (2007). *Rev. Sci. Instrum.* **78**, 025102.

Pierce, D. T. (1995). *Spin Polarized Electron Sources* in *Experimental Methods in the Physical Sciences*, edited by F. B. Dunning & R. G. Hulet. New York: Academic Press.

Pierce, D. T., Girvin, S. M., Unguris, J. & Celotta, R. J. (1981). *Rev. Sci. Instrum.* **52**, 1437–1444.

Pirbhai, M., Ryan, D. M., Richards, G. & Gay, T. J. (2013). *Rev. Sci. Instrum.* **84**, 053113.

Rodionov, A. A., Golyashov, V. A., Chistokhin, I. B., Jaroshevich, A. S., Derebezov, I. A., Haisler, V. A., Shamirzaev, T. S., Marakhovka, I. I., Kopotilov, A. V., Kislykh, N. V., Mironov, A. V., Aksenov, V. V. & Tereshchenko, O. E. (2017). *Phys. Rev. Appl.* **8**, 034026.

Sawler, J. & Venus, D. (1991). *Rev. Sci. Instrum.* **62**, 2409–2418.

Schnitzer, I., Yablonovitch, E., Caneau, C. & Gmitter, T. J. (1993). *Appl. Phys. Lett.* **62**, 11.

Schönhense, G. & Siegmann, H. C. (1993). *Ann. Phys.* **505**, 465–474.

Strocov, V. N., Petrov, V. N. & Dil, J. H. (2015). *J. Synchrotron Rad.* **22**, 708–716.

Suga, S. & Tusche, C. (2015). *J. Electron Spectrosc. Relat. Phenom.* **200**, 119–142.

Tereshchenko, O. E., Chikichev, S. I. & Terekhov, A. S. (1999). *J. Vac. Sci. Technol. A*, **17**, 2655–2662.

Tereshchenko, O. E., Golyashov, V. A., Eremeev, S. V., Maurin, I., Bakulin, A. V., Kulkova, S. E., Aksenov, M. S., Preobrazhenskii, V. V., Putyato, M. A., Semyagin, B. R., Dmitriev, D. V., Toropov, A. I., Gutakovskii, A. K., Khandarkhaeva, S. E., Prosvirin, I. P., Kalinkin, A. V., Bukhtiyarov, V. I. & Latyshev, A. V. (2015). *Appl. Phys. Lett.* **107**, 123506.

Tereshchenko, O. E., Golyashov, V. A., Rodionov, A. A., Chistokhin, I. B., Kislykh, N. V., Mironov, A. V. & Aksenov, V. V. (2017). *Sci. Rep.* **7**, 16154.

Tereshchenko, O. E., Lamine, D., Lampel, G., Lassailly, Y., Li, X., Paget, D. & Peretti, J. (2011). *J. Appl. Phys.* **109**, 113708.

Tereshchenko, O. E., Paulish, A. G., Neklyudova, M. A., Shamirzaev, T. S., Yaroshevich, A. S., Prosvirin, I. P., Zhaksylykova, I. E., Dmitriev, D. V., Toropov, A. I., Varnakov, S. N., Rautskii, M. V., Volkov, N. V., Ovchinnikov, S. G. & Latyshev, A. V. (2012). *Tech. Phys. Lett.* **38**, 12.

Tereshchenko, O. E., Shaibler, G. E., Yaroshevich, A. S., Shevelev, S. V., Terekhov, A. S., Lundin, V. V., Zavarin, E. E. & Besyul'kin, A. I. (2004). *Phys. Solid State*, **46**, 1949–1953.

Thiede, C., Langenkämper, C., Shirai, K., Schmidt, A. B., Okuda, T. & Donath, M. (2014). *Phys. Rev. Appl.* **1**, 054003.

Tillmann, D., Thiel, R. & Kisker, E. (1989). *Phys. B: Condens. Matter*, **77**, 1–2.

Trantham, K. W., Gay, T. J. & Vandiver, R. J. (1996). *Rev. Sci. Instrum.* **67**, 4103–4108.
Tusche, C., Ellguth, M., Feyer, V., Krasyuk, A., Wiemann, C., Henk, J., Schneider, C. M. & Kirschner, J. (2018). *Nat. Commun.* **9**, 3727.
Tusche, C., Ellguth, M., Ünal, A. A., Chiang, C.-T., Winkelmann, A., Krasyuk, A., Hahn, M., Schönhense, G. & Kirschner, J. (2011). *Appl. Phys. Lett.* **99**, 032505.
Vasilyev, D., Medjanik, K., Babenkov, S., Ellguth, M., Schönhense, G. & Elmers, H.-J. (2020). *J. Phys. Condens. Matter*, **32**, 135501.
Vasilyev, D., Tusche, C., Giebels, F., Gollisch, H., Feder, R. & Kirschner, J. (2015). *J. Electron Spectrosc. Relat. Phenom.* **199**, 10–18.
Wang, G.-C., Celotta, R. J. & Pierce, D. T. (1981). *Phys. Rev. B*, **23**, 1761–1770.
Weber, W., Riesen, S. & Siegmann, H. C. (2001). *Science*, **291**, 1015–1018.
Yu, D., Math, C., Meier, M., Escher, M., Rangelov, G. & Donath, M. (2007). *Surf. Sci.* **601**, 5803–5808.